Direct magneto-optical compression of an effusive atomic beam for high resolution focused ion beam application

Direct magneto-optical compression of an effusive atomic beam for high resolution focused ion beam application

G. ten Haaf,* T.C.H. de Raadt, G.P. Offermans, J.F.M. van Rens, P.H.A. Mutsaers, E.J.D. Vredenbregt,† and S.H.W. Wouters*
Department of Applied Physics, Eindhoven University of Technology, P.O. Box 513, 5600 MB Eindhoven, the Netherlands
(Dated: December 7, 2016)

An atomic rubidium beam formed in a 70 mm long magneto-optical compressor, directly loaded from a collimated Knudsen source, is analyzed using laser-induced fluorescence. The longitudinal velocity distribution, the transverse temperature and the flux of the atomic beam are reported. The equivalent transverse reduced brightness of an ion beam with similar properties as the atomic beam is calculated because the beam is developed to be photoionized and applied in a focused ion beam. In a single magneto-optical compression step an equivalent transverse reduced brightness of $(1.0^{+0.8}_{-0.4}) \times 10^6$ A/(m^2 sr eV) was achieved with a beam flux equivalent to $(0.6^{+0.3}_{-0.2})$ nA. The temperature of the beam is further reduced by applying sub-Doppler cooling behind the magneto-optical compressor. This increased the equivalent brightness to $(6^{+5}_{-2}) \times 10^6$ A/(m^2 sr eV). When fully ionized this will be a six times improvement over the liquid metal ion source, which would improve the resolution in focused ion beam nanofabrication.

PACS numbers: 37.20.+j,07.77.Ka,89.20.Bb

I. INTRODUCTION

Laser cooling and compression is used to intensify atomic beams for use in a variety of physics experiments such as loading of magneto-optical traps (MOTs), beam collision studies [1] and atom interferometry [2]. In most of these experiments the aim is to get a high flux of slowly propagating atoms or atoms with a low longitudinal velocity spread. There are two common routes in realizing this. One can capture atoms from the background vapour in a so called 2D$^+$ MOT [3, 4], or one can start out with an effusive source, use a Zeeman slower to slow down the atoms and then cool and compress the atoms in the transverse direction [5, 6].

A new field of application is the ionization of such atomic beams to create high brightness ion beams [7]. These beams can be applied in a focused ion beam (FIB), a table top instrument in which nanoscale devices can be inspected, by gathering secondary electrons or ions, and fabricated, by etching and ion beam induced deposition [8, 9]. For these applications the most important figures of merit are the transverse reduced brightness and the energy spread of the ion beam, as these determine the FIBs resolution together with parameters of the electrostatic lens column. The ion source mostly used in commercial FIBs for high resolution nanofabrication purposes is currently the liquid metal ion source (LMIS). This source offers a reduced transverse brightness of 10^6 A/(m^2 sr eV) [10] and a full width at half maximum energy spread of 4.5 eV [11]. With this beam quality a LMIS based FIB has a resolution of roughly 5 nm when operated at 30 kV with a beam current of 1 pA [12].

Several research groups worldwide have been working on ion sources based on the field- or photoionization of cold atoms. The first realizations [13, 14] consist of a magneto-optical trap from which the ions are created and extracted. The ion current, and therefore also the reduced brightness, from these sources is limited by the slow refilling rate of the ionization volume inside the MOT. Several proposals [15–18] have been made to overcome this problem by creating a cold atomic beam instead of a MOT, which is subsequently ionized. Knuffman et al. realized a cold cesium ion source in which atoms are captured from the background vapour and transversely cooled and compressed in three steps after which they are ionized [16]. Another way to create the atomic beam is to start out with a thermal source and transversely cool and compress the atoms effusing from it, which is the strategy followed in the atomic beam laser-cooled ion source (ABLIS), which is discussed in this paper. Extensive simulations of this source predict that when combined with a conventional electrostatic focusing column, 1 pA of 30 keV rubidium ions can be focused to a 1 nm spot [18, 19]. Recently, other researchers realized an ion microscope which was based on the field ionization of a transversely cooled thermal beam of cesium atoms [17, 20].

In this paper the experimental verification of the atomic beam creation in the earlier mentioned ABLIS setup is discussed. In this setup, rubidium atoms from a collimated Knudsen source [21] are cooled in the transverse direction and also compressed. As the source is intended to be mounted on a FIB system it should be compact. Therefore the atoms are immediately cooled and compressed after exiting the Knudsen source, without any Zeeman slowing. The quality of the beam after a single magneto-optical compression step is analyzed. The improvement of the beam with an additional op-

* authors contributed equally to this paper
† e.j.d.vredenbregt@tue.nl

tical molasses step is also explored. The longitudinal velocity distribution, beam flux and transverse temperature are measured using laser-induced fluorescence (LIF). Also, the equivalent transverse reduced brightness is determined, which is defined as the brightness of an ion beam with similar temperature and flux density as the atomic beam. Section II describes the experimental setup in which this is done and the methods used after which all experimental results are presented in section III and section IV presents the conclusions.

II. METHODS

In the experiment, schematically shown in figure 1, an atomic rubidium beam from a collimated Knudsen source [21] with temperature T_s effuses into a magneto-optical compressor (MOC) [22]. After the MOC the atoms can be cooled to sub-Doppler temperature with a second set of counter propagating laser beams. After a 0.2 m drift, a probe laser beam is used to visualize the atomic beam by means of laser-induced fluorescence (LIF) which is imaged onto a camera. From the divergence of the atomic beam the temperature is calculated while the intensity of the LIF signal allows the determination of the flux of the beam. Both of these calculations require knowledge about the longitudinal velocity distribution of the atoms in the beam. By placing the probe under an angle with respect to the atomic beam and scanning its frequency, this distribution is determined.

The remainder of this methods section is divided into three parts. First the details of the experimental setup are described. Then the methods to determine the flux, transverse temperature and equivalent transverse reduced brightness are introduced and finally the method to measure the longitudinal velocity distribution will be explained.

A. Experimental setup

The compact MOC consists of an in-vacuum electromagnet with a pure iron core, capable of creating a two dimensional quadrupole field with a magnetic field gradient ∇B of 3.8 T/m. Four identical laser beam expansion modules (not shown in the figure) generate the required laser fields with a σ^+/σ^- polarization scheme and a $1/e^2$ diameter of 12 mm in the transverse direction (x or y) and 120 mm in the longitudinal (z) direction. The peak intensity of each of the four MOC beams is 98 W/m^2. The yoke of the magnet has 70 mm long slots milled into it to allow the laser beams to reach the center.

Downstream of the MOC laser beams, there is a 10 mm long drift space in which the atoms do not see laser light and in which the magnetic field (gradient) decreases. At the end of the yoke a μ-metal plate is placed to shield the region behind the yoke from magnetic fields to allow for additional sub-Doppler cooling. Directly behind the μ-metal plate an aperture with a 100 μm diameter is placed for beam selection. An imbalance is made in the currents through the four coils of the quadrupole magnet to steer the atomic beam through the selection aperture. A sub-Doppler after cooling stage is placed directly behind the selection aperture. Here, a pair of counter propagating laser beams is applied in both transverse directions. These laser beams have a $1/e^2$ diameter of 12 mm and a peak intensity of 1.5×10^2 W/m^2. The polarizations of these laser beams are chosen such that in both directions a lin-perp-lin configuration was achieved.

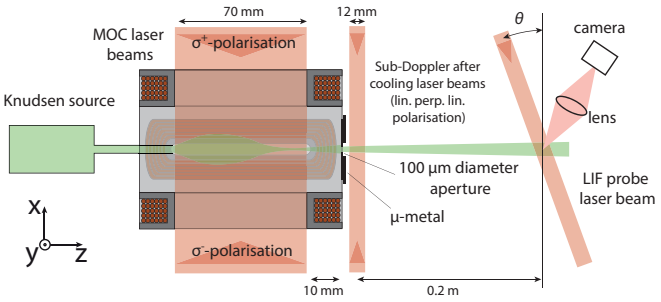

FIG. 1. Overview of the experimental setup (not drawn to scale). An atomic rubidium beam effusing from a collimated Knudsen source is cooled and compressed by means of two sets of σ^+/σ^- polarized laser beams and a compact in-vacuum quadrupole electromagnet with an iron core. A μ-metal plate shields the region behind the electro-magnet from magnetic fields and an aperture selects the central part of the beam. The atomic beam is allowed to drift for 0.2 m where its profile is imaged onto a camera using laser-induced fluorescence. The probe beam can be rotated to make an angle θ with the transverse direction of the atomic beam in order to the determine the longitudinal velocity distribution.

Laser-induced fluorescence is used to determine the important atomic beam properties. At a distance of $\Delta z = 0.20$ m from the beam selection aperture, a probe laser beam propagating over the line $x = y$ is crossed with the atomic beam. This probe beam has a $1/e^2$ diameter of 11.5 mm, is linearly polarized in the z-direction and has a peak intensity of 1.9 W/m^2 in the longitudinal velocity distribution measurements and 96 W/m^2 in all other measurements shown. The fluorescent light emitted by the atoms is imaged onto two cameras [23]; one looking at the beam in the x-direction and one in the y-direction. Both images are made with two best-form lenses providing a 2.3× de-magnification. This allows the determination of the temperature of the atomic beam in both transverse directions. A coloured glass filter is placed in front of the cameras to reduce the influence of background light. Each measurement series is started with a camera image with the probe laser far detuned. This image is subtracted from all other images in the measurement to correct for background scattering.

The cooling (and after-cooling) laser light is generated using a Coherent 899-21 Ti:Saph ring laser. This laser is frequency stabilized at the cross-over resonance between the $5\,^2S_{1/2}F = 3$ to $5\,^2P_{3/2}F' = 2, 4$ transitions of

rubidium-85 in the frequency modulation spectrum [24]. An acousto-optical modulator in double pass configuration is used to shift the laser frequency to the desired detuning δ from the $5\,^2\mathrm{S}_{1/2}\mathrm{F} = 3$ to $5\,^2\mathrm{P}_{3/2}\mathrm{F}' = 4$ cooling transition. A resonant electro-optical modulator is used to generate sidebands at ±2915 MHz, of which the positive sideband is used for repumping. The cooling and repumping light is coupled into a polarization maintaining fiber that splits in four and connects to the optical modules that shape the laser beams for the MOC and the sub-Doppler after cooling. An acousto-optical modulator placed before the fiber-coupler is used to stabilize the power in the cooling and after-cooling beams. The light in the probe laser beam is generated using a Toptica DL100-XXL diode laser. This laser is frequency stabilized by means of a frequency offset servo [25] that keeps the frequency difference within 100 Hz of the desired difference with respect to the Ti:Saph laser frequency. Varying the set point of this system allows setting the probe laser detuning δ_p within a range of -90 to 100 MHz.

B. Beam flux, temperature and brightness

In this section the equations are presented with which the temperature, flux and equivalent brightness of the atom beam are extracted from the LIF measurements. A simple model is set up to describe the transverse density profile of the beam after the drift from the selection aperture to the probe laser beam. This profile depends on the velocity distribution of the atoms, so it can be used to determine the transverse temperature of beam. Also the equations to determine the atomic flux and density of the beam from the intensity of the LIF signal are given. Finally the relations between flux, temperature and equivalent brightness are presented.

After an atom drifts over a length Δz, its transverse position x_2 is given by $x_2 = x_1 + \Delta z\, v_x/v_z$, in which x_1 is the initial transverse position, v_x is the transverse velocity and v_z is the longitudinal velocity of the atom. Assuming x_1, v_x and v_z are uncorrelated and v_x is distributed according a normal distribution with root-mean-square (rms) width σ_{v_x}, the mean square size of the distribution in x_2 is given by,

$$\langle x_2^2\rangle = \langle x_1^2\rangle + (\Delta z)^2\,\sigma_{v_x}^2\langle 1/v_z^2\rangle, \tag{1}$$

and the transverse temperature T_x of the beam can be written as

$$T_x = \frac{m\,\sigma_{v_x}^2}{k_\mathrm{B}} = \frac{m}{k_\mathrm{B}}\left(\frac{\widetilde{v_z}}{\Delta z}\right)^2\left(\langle x_2^2\rangle - \langle x_1^2\rangle\right), \tag{2}$$

in which m is the mass of the atom [26], k_B is Boltzmann's constant and $\widetilde{v_z} = 1/\sqrt{\langle 1/v_z^2\rangle}$. Finding the transverse temperature now relies on measuring $\langle x_2^2\rangle$. Under the assumption that all the atoms are resonant with the probe laser, the LIF profile will have the same width as the distribution of x_2. This requires that the Doppler shift of the atoms due to their transverse velocity is smaller than the linewidth Γ [26] of the transition, i.e. $2\pi\sigma_{v_x}/\lambda < \Gamma$ in which λ is the wavelength of the transition. This assumption is valid for transverse beam temperatures lower than 0.2 K which is easily achieved in the experiment. The initial position x_1 is assumed to be uniformly distributed over the circular selection aperture. Such a distribution gives $\langle x_1^2\rangle = R/2$, in which R is the radius of the selection aperture. As will be shown later, this value is significantly smaller than the spread due to the divergence of the beam due to which the distribution in x_2 resembles a normal distribution very well. Therefore $\langle x_2^2\rangle$ is found by fitting such a distribution to the LIF profile.

The scattering rate of LIF photons R_ph can be found from the intensity C of the LIF signal. C is acquired by calculating the area under the normal distribution fitted through the LIF profile and is expressed in camera counts. Using its value, R_ph can be calculated with

$$R_\mathrm{ph} = \frac{C}{G\,t_\mathrm{c}\,T_\mathrm{geom}\,T_\mathrm{w}\,T_\mathrm{f}} \tag{3}$$

in which G is the number of counts measured by the camera per incident photon, t_c is the shutter time of the camera, $T_\mathrm{geom} = \pi r_\mathrm{l}^2/(4\pi o^2)$ is the part of the isotropic emission sphere that the imaging lens with radius r_l at a distance o from the atomic beam covers and T_w and T_f are the transmission of the vacuum window and the colour filter. The beam flux Φ is calculated from the scattering rate using

$$\Phi = \frac{R_\mathrm{ph}}{\langle t_\mathrm{tr}\rangle \rho_{ee}\,(0)\;\Gamma}, \tag{4}$$

in which $\langle t_\mathrm{tr}\rangle$ is the average transfer time through the imaging volume and $\rho_{ee}\,(\delta_p)$ is the excited state population as a function of the probe laser detuning δ_p, which is given by [27]

$$\rho_{ee}\,(\delta_p) = \frac{\frac{s_0}{2}}{1 + s_0 + \left(\frac{2\delta_p}{\Gamma}\right)^2}, \tag{5}$$

where $s_0 = I/I_{sat}$ is the saturation parameter, in which I is the laser beam intensity and I_{sat} is the saturation intensity [26]. Note that in the determination of the transverse temperature, the probe detuning is set to zero. The average transfer time through the imaging volume is given by $\langle t_\mathrm{tr}\rangle = l/\overline{v_z}$, in which l is the longitudinal width of the imaged volume and $\overline{v_z} = 1/\langle 1/v_z\rangle$.

If all atoms are ionized, which is possible in a two-step ionization process and using a build-up cavity for the ionization laser light [18], the beam current will be $I = e\Phi$ in which e is the elementary charge. With the intended application of the beam in a FIB system in mind, the measured flux will be reported in the unit Ampere as an equivalent ion current throughout this paper.

Instead of the beam flux, the average beam density n at the selection aperture, can be calculated using

$$n = \frac{R_\mathrm{ph}}{\pi R^2\, l\,\rho_{ee}\,(0)\;\Gamma}. \tag{6}$$

Note that this quantity can be determined without knowing the longitudinal velocity of the atoms.

Assuming there are no correlations between x and v_x and y and v_y at the position of the selection aperture, that the atoms are uniformly distributed over this circular selection aperture and that v_x and v_y are distributed according to a normal distribution, the transverse reduced brightness of an ion beam with equal properties to that of the atomic beam can be calculated with [28]

$$B_r = \frac{e\,\Phi}{\pi^2 R^2\, k_\mathrm{B} \sqrt{T_x\, T_y}}. \tag{7}$$

Note that if there are correlations between transverse position and velocity at the selection aperture, the equivalent brightness will be higher than this calculated value. Furthermore, if the atoms are not uniformly distributed over the aperture the brightness will be higher as well. This means the calculated value is a lower limit of the actual peak equivalent brightness. As a last remark, note that for presenting the number from equation 7 in the unit of $\mathrm{A}/(\mathrm{m}^2\,\mathrm{sr}\,\mathrm{eV})$ multiplication by a second factor e is required.

An estimate of systematic uncertainties in the experiment was made (see the Appendix). Due to the many factors involved in the scattering, collection and conversion of LIF photons, error margins for the temperature ($^{+62}_{-37}\,\%$), flux ($^{+51}_{-32}\,\%$), density ($^{+48}_{-31}\,\%$) and brightness ($^{+80}_{-38}\,\%$) are quite substantial.

C. Longitudinal velocity distribution

In the calculation of all important beam parameters the value of either $\overline{v_z}$ or $\widetilde{v_z}^2$ plays an important role. As can be seen in equations 2 and 4 the measured temperature scales with $\widetilde{v_z}^2$ and the measured flux with $\overline{v_z}$. As shown by equation 7 this means that the measured brightness scales with with $\overline{v_z}/\widetilde{v_z}^2$. One could assume that the longitudinal velocity of the atoms in the beam is distributed according to a Maxwell-Boltzmann distribution with the temperature of the source T_s. However, due to the finite length of the MOC it is to be expected that atoms with a higher longitudinal velocity are laser-cooled less effectively and thus have a lower probability of being transmitted through the selection aperture. Therefore the values of $\overline{v_z}$ and $\widetilde{v_z}^2$ are acquired experimentally to prevent any errors in the determination of the beam quality due to a wrongly estimated longitudinal velocity.

The longitudinal velocity distribution $p\,(v_z)$ is determined by looking at the intensity $F\,(\delta_p)$ of the fluorescence signal as a function of the detuning of the probe laser beam that is now oriented so that it makes an angle $\theta = 14.8°$ with the atomic beam, see figure 1. In this way the longitudinal velocity of the atoms will cause a Doppler shift in the frequency of the laser, so that the effective detuning becomes $\delta_p - k v_z \sin\theta$. Therefore, $F\,(\delta_p)$ becomes dependent on the longitudinal velocity of the atoms. This can be expressed in a proportionality given by

$$F\,(\delta_p) \propto \int_0^\infty \frac{p\,(v_z)}{v_z} \rho_{ee}\,(\delta_p - k v_z \sin\theta)\,\mathrm{d}v_z, \tag{8}$$

which explicitly includes all dependence on the longitudinal velocity of the atoms. It shows that $F\,(\delta_p)$ is a convolution of the line shape of the transition with $p\,(v_z)\,/v_z$, in which the extra factor of $1/v_z$ compensates for the fact that the transfer time through the imaged volume is smaller for faster traveling atoms which therefore contribute less to the fluorescence than slower traveling atoms.

To find $p\,(v_z)$, the measured data needs to be deconvoluted from the linewidth of the transition. Since numerical deconvolution is difficult, the data was fitted with a test function, that represented $p\,(v_z)\,/v_z$, which was convoluted with $\rho_{ee}\,(\delta_p)$. For the test function a sixth order polynomial $P_6\,(v_z)$ was chosen, multiplied by a Gaussian distribution $e^{-\frac{v_z^2}{a^2}}$, in which a is a fitting parameter and $P_6\,(v_z)$ contains the other seven fitting parameters. This means that after fitting the data, $p\,(v_z)$ is calculated with

$$p\,(v_z) = C_n v_z P_6\,(v_z)\, e^{-\frac{v_z^2}{a^2}}, \tag{9}$$

in which C_n is a normalization constant. The resulting distribution is finally used to calculate the required moments $\overline{v_z}$ and $\widetilde{v_z}^2$.

Note that the test function in this fitting routine is not based on any physical argument. Since the goal was not to find an analytical expression for the distribution but to deconvolute the measured data from the linewidth of the transition, a test function with a large number of fitting parameters was chosen that gives a precise fit to the measured data. The chosen test function does make sure that the distribution goes to zero in the limits of v_z to zero and to infinity.

III. RESULTS

In this section the measurements of the atomic beam parameters are discussed. As the values of $\overline{v_z}$ and $\widetilde{v_z}^2$ are needed in order to calculate the equivalent brightness of the beam the longitudinal velocity distribution measurement is discussed first.

A. Longitudinal velocity distribution

Figure 2 shows an example of a longitudinal velocity distribution measurement. The measured data was fitted as described in subsection II C. As can be seen the large number of fitting parameters enables a good fit with the data. The normalized longitudinal velocity distribution that was obtained from this measurement is plotted in figure 3. The distribution yields an average velocity of

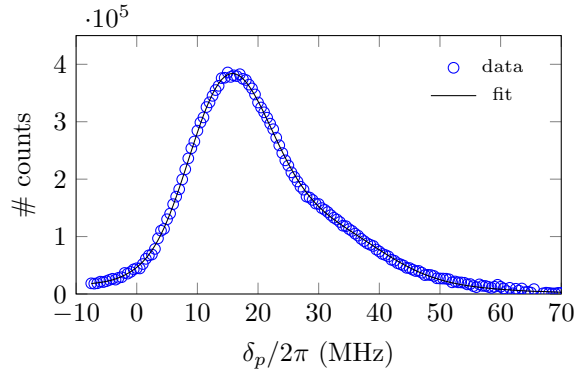

FIG. 2. Laser Induced fluorescence signal as a function of the laser detuning. The laser made an angle $\theta = 14.8^\circ$ with the transverse direction of the atomic beam. To extract the longitudinal velocity distribution the data was fitted with a sixth order polynomial that was multiplied with a Gaussian and convoluted with equation 5. This measurement was performed with $\nabla B = 0.94$ T/m, $\delta = -1.1\,\Gamma$ and $T_s = 433$ K.

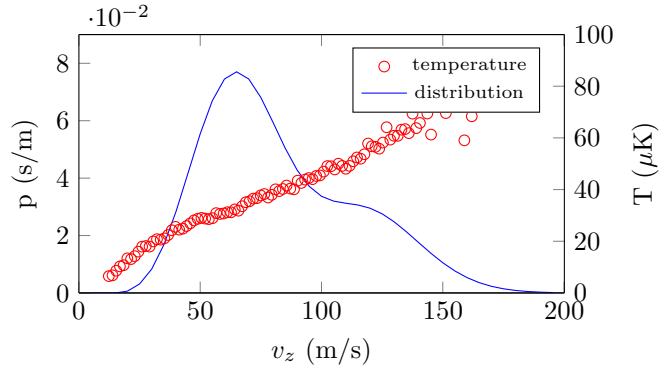

FIG. 3. Longitudinal velocity distribution and a plot of the transverse temperature against the longitudinal velocity. The longitudinal velocity distribution is found from the data plotted in figure 2. The measurement was performed with $\theta = 14.8^\circ$, $\nabla B = 0.94$ T/m, $\delta = -1.1\,\Gamma$ and $T_s = 433$ K.

83 m/s. This is much smaller than the average velocity of the thermal atoms in the Knudsen source which is 330 m/s.

As figure 3 results from a deconvolution it is important to mention that features within a velocity span of approximately $\Gamma/k \sin\theta = 18$ m/s are washed out and not properly represented in the velocity distribution found. Nevertheless there are some distinct features that are apparent in the distribution. There are no atoms with a velocity below $\approx$ 20 m/s. Part of the explanation for this lies in the fact that the atoms travel through a region of 10 mm with no laser cooling and compression before being selected by the selection aperture. The slower the atoms travel longitudinally the larger the divergence of these atoms will be in this region, which lowers the probability of being transmitted through the aperture. Furthermore, after the selection aperture, slower traveling atoms will also have a larger divergence which means that they are more spread out at the position where they

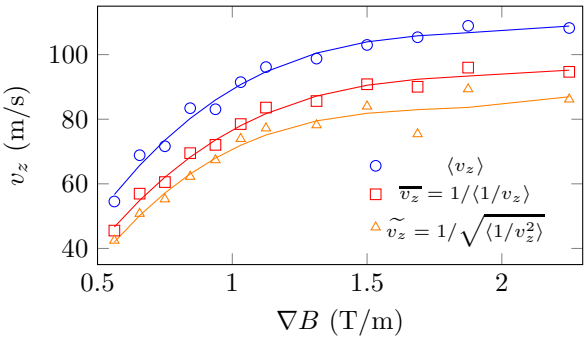

FIG. 4. Several moments of the longitudinal velocity distribution as a function of the magnetic field gradient. The fit is performed with a third order polynomial. This fit function has no physical meaning, but serves as a guide to the eye in this figure. The data was measured with $\delta = -1.1\,\Gamma$ and $T_s = 433$ K.

were imaged. Therefore their fluorescence is less intense and at low enough velocities becomes smaller than the noise level in the images. After the maximum of the distribution there appears to be a second hump, which is found to be more pronounced at larger magnetic field gradients. The reason for this feature is not known.

Similar measurements have been performed at different magnetic field gradients. Figure 4 shows the average velocity and the two moments required in the calculation of the reduced brightness as a function of the magnetic field gradient. Below 0.5 T/m the fluorescence signal was not high enough to perform reliable measurements. Between 0.5 T/m and 1.5 T/m the averages increase, which can be explained by the fact that by increasing the magnetic field gradient the spring constant of the compression becomes larger. This larger spring constant enables compression of faster traveling atoms that did not have enough time to be pushed to the axis at lower gradients. Above a gradient of 1.5 T/m the averages do not change much. The values of $\overline{v_z}$ and $\widetilde{v_z}^2$ are used to calculate the flux, temperature and the equivalent reduced brightness in the next section. Instead of interpolating between measured values, the data shown in figure 4 was fitted with a third order polynomial in order to get values for $\overline{v_z}$ and $\widetilde{v_z}^2$ at magnetic field gradients between 0.5 and 2.5 T/m.

In the derivation of equation 2 the assumption was made that no correlation exists between v_x and v_z. In this measurement of the longitudinal velocity distribution it is possible to check to what extent this approximation is valid. This is done by looking at the divergence of different velocity groups in the atomic beam, i.e., by also determining the rms size of the beam at each detuning and using equation 2 to determine the temperature in which now $\delta_p/k \sin\theta$ was used for the longitudinal velocity instead of $\widetilde{v_z}$. The results are shown in figure 3. As can be seen, slower traveling atoms are cooled to a lower temperature than faster traveling atoms, which was to be

expected due to the longer time they interact with the after cooling laser. Calculating the average of the temperature weighted over the longitudinal velocity distribution yields a value of 40 μK. A measurement performed according the method described in subsection II B also gave this value. This shows that although there does exist a correlation between the transverse and longitudinal velocity, equation 2 yields a reliable value of the temperature of the beam.

B. Beam profiles

Figure 5 shows several transverse fluorescence profiles of the atomic beam. In the measurements shown in the top panel the after cooling laser beams were turned off while for the bottom figure they were enabled. As is apparent from the figures, increasing the magnetic field gradient increases the intensity of the LIF signal. In the MOC only case it also leads to a broader profile. At high magnetic field gradients the after cooled profiles have a smaller width than the profiles in the MOC only case, indicating that the divergence of the beam is indeed reduced. Careful analysis of the profiles teaches that for the MOC only case the center of the profiles do not overlap for different magnetic field gradients. They are also slightly asymmetric. Both of these observations are attributed to the steering by means of making an imbalance in the currents through the coils of the magnetic quadrupole. By creating an imbalance, the magnetic axis (where $B = 0$) can be overlapped with the selection aperture. However, by doing this, the pointing of the atomic beam is altered as well. With the after cooling laser beams enabled this effect does not occur since after the selection aperture the atoms are cooled again and this configuration does not change when changing the magnetic field gradient. The figures also show the Gaussian fits through the profiles, which are used for further analysis. In the case with the after cooled lasers enabled, the fits overlap nicely with the data. Due to the asymmetries in the profiles the overlap is less satisfactory without after cooling, but still good enough for analysis of the beam properties.

C. Effect of cooling laser detuning

An important parameter in the laser cooling and compression process is the detuning of the cooling laser. A large negative detuning results in a large capture velocity but a small damping rate of the velocity of the atoms whereas a small negative detuning results in a small capture velocity but a high damping rate [27]. To find the optimum in this trade-off, the detuning was varied and the LIF intensity and profile were monitored. Figure 6 shows the results of this experiment in which the after cooling lasers were disabled. The absolute frequency of the cooling laser was not determined accurately so the

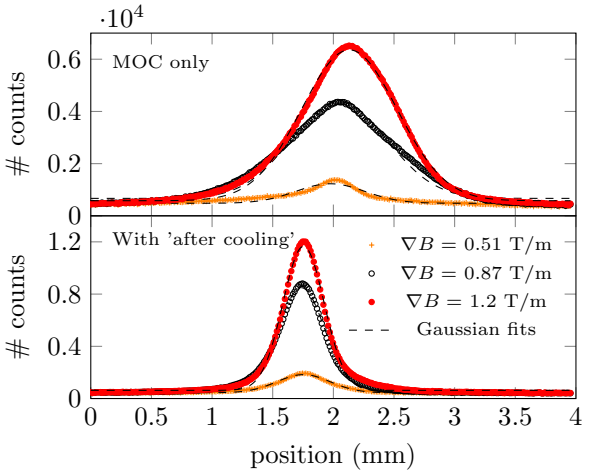

FIG. 5. Transverse beam profiles (dots, circles and plusses) after the drift of 0.20 m in the case with (bottom) and without (top) after cooling. The profiles are shown for different magnetic field gradients. The figure also shows the Gaussian fits (dashed lines) which were used for analysis of the temperature, flux and equivalent brightness of the beam. The data was measured with $\delta = -1.1\,\Gamma$ and $T_s = 413$ K.

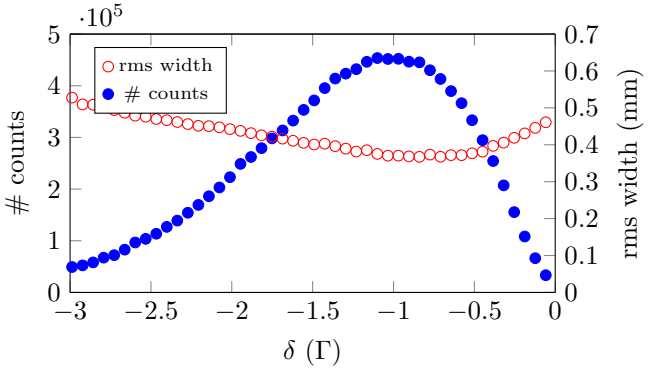

FIG. 6. Total LIF intensity and rms beam width after 0.2 m drift as a function of the detuning of the cooling laser. The data was measured with $\nabla B = 1.2$ T/m and $T_s = 413$ K.

detuning axis was shifted in such a way that no counts where achieved at δ=0. The results confirm the trade-off between capture velocity and damping rate. The LIF signal increases from δ=0 to δ =-1.1 Γ, indicating the density at the selection aperture increases. Decreasing the detuning further from δ=-1.1 Γ reduces the LIF signal again. The rms width also shows the trade-off: lowering the detuning leads to a decrease, a minimum is achieved at δ=-0.8 Γ and lowering the detuning even further increases the rms width again. In an infinitely long laser cooler (no compression) with near-zero saturation intensity the lowest temperature is reached at δ=-Γ/2. Due to the finite length of the MOC, the compression and the high saturation parameter, optimum flux and temperature in the experiment were reached at a different detuning. All other measurements shown were therefore carried out at δ=-1.1 Γ.

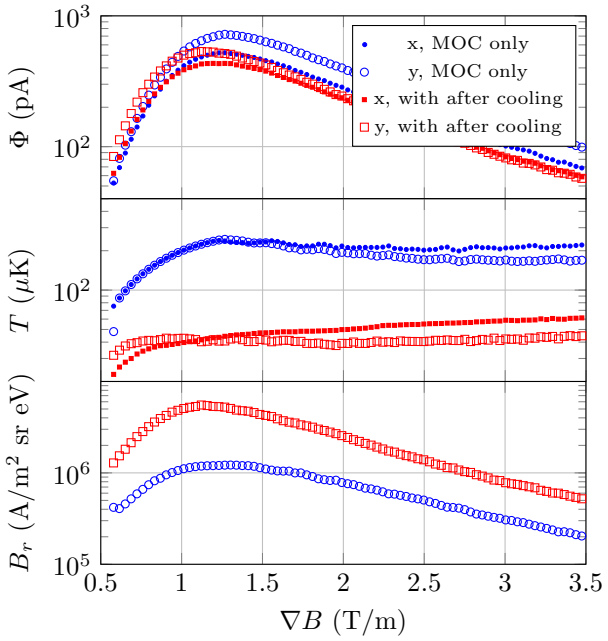

FIG. 7. Flux, transverse temperature and equivalent brightness of the atomic beam as a function of different magnetic field gradients. The results with (squares) as well as the results without (circles) after cooling laser beams are shown. In the upper graph the flux as calculated from both of the cameras is shown. In the calculation of the equivalent brightness in the lower graph the average of the two measured fluxes is used. The data was measured with T_s=413 K and δ=-1.1 Γ.

D. Effect of the magnetic field gradient

Another important parameter determining the properties of the atomic beam is the magnetic field gradient. Similarly as the detuning, a small magnetic field gradient leads to a large capture range but a small spring constant [27], pulling the atoms towards the magnetic axis. On the other hand, a high magnetic field gradient leads to a small capture range but a high spring constant. Furthermore, the presence of a magnetic field can inhibit sub-Doppler cooling mechanisms that occur due to the σ^+/σ^- laser beam configuration. Figure 7 shows the flux, transverse temperature and equivalent brightness as a function of the magnetic field gradient for the case with as well as without after cooling. The longitudinal velocity distribution was only measured for magnetic field gradients in the range 0.5-2.5 T/m. Since $\overline{v_z}$ and $\widetilde{v_z}$ are needed in the calculation of all the parameters shown, they are not determined below 0.5 T/m. Because of the trend shown in figure 4, $\overline{v_z}$ and $\widetilde{v_z}$ are assumed to be constant and equal to their values at 2.5 T/m, for values above this magnetic gradient.

In the top graph the beam flux through the selection aperture is shown in units of Ampere, resembling the maximum ion current that can be made from the atomic beam. It shows separate values for the x- and y-direction, which were calculated using the data taken with the two different cameras. They differ by approximately 20%. As expected, the flux increases when the magnetic field gradient is raised and decreases again after reaching an optimum. The highest flux, equivalent to $\left(0.5^{+0.3}_{-0.2}\right)$nA, was achieved at a magnetic field gradient of 1.2 T/m. Since there is no further selection after the after cooling section there is no significant difference in flux in the cases with and without after cooling.

The middle graph shows the transverse temperature plotted as a function of the magnetic field gradient. In the MOC only case the lowest temperature was measured at ∇B=0.6 T/m and equals $\left(0.07^{+0.04}_{-0.03}\right)$ mK. Furthermore, the trend indicates even lower temperatures at lower magnetic field gradients. The measured temperature is below the Doppler temperature of rubidium (0.143 mK) suggesting that sub-Doppler cooling effects do play a role, even in the presence of a magnetic field. Increasing the magnetic field gradient results in a higher temperature, stabilizing at $\left(0.2^{+0.1}_{-0.07}\right)$ mK which is near the Doppler temperature. Note that the lowest temperature and highest flux are not achieved at the same magnetic field gradient. With the after cooling laser enabled, the temperature does not change significantly in the measured range and is equal to $\left(0.04^{+0.02}_{-0.01}\right)$ mK.

The bottom graph shows the equivalent brightness of the atomic beam. It was determined by averaging the fluxes calculated from the x and y cameras and using the temperature as acquired from both cameras. For the MOC only case the highest brightness reads $(1.0^{+0.8}_{-0.4}) \times 10^6$ A/(m² sr eV) at a magnetic field gradient of 1.2 T/m. Due to the lower temperature the equivalent brightness is higher with the after cooling laser enabled and reads $(5^{+5}_{-2}) \times 10^6$ A/(m² sr eV). As was calculated previously [18, 19], the atomic beam can be ionized and accelerated without major heating. Therefore the resulting ion source would be an improvement over the current state-of-the art LMIS in terms of ion beam brightness.

E. Beam density vs. source temperature

The last parameter that was varied is the temperature of the Knudsen source. Under the assumption of no collisions or other density limiting effects, increasing the temperature of the source would lead to an increase in flux according to equations 1 and 12 from [18]. However it is known from experiments on magneto-optical traps that at high densities and intense resonant illumination, inelastic collisions between ground and excited state atoms [29] and attenuation and radiation trapping effects [30] will limit the achievable density. Therefore an experiment was performed in which the temperature of the Knudsen source was varied.

Figure 8 shows the beam density as a function of source temperature in two cases: with the magnetic field gradient set to the optimal value of 1.1 T/m and without any magnetic field. The figure also shows a scaling law that scales the first data point of both measurements

with the flux coming from the Knudsen source [21]. Although the beam density does increase with increasing source temperature, figure 8 shows that the scaling law only holds for the lowest temperatures and in the case of no magnetic field gradient. At the highest temperature the measurement and the scaling are off by a factor 11 in the case without a magnetic gradient and a factor 21 in the case with a magnetic gradient. This deviation from the scaling can be attributed to three effects. First of all, in the determination of total flux of atoms effusing from the collimated Knudsen source, see ref [18], it was observed that at high temperatures the flux was lower than expected from the model. At 433 K the difference is a factor 2, partly explaining the difference in this experiment. In the measurement of the flux from the collimated Knudsen source it was also observed that the transverse velocity distribution of the atoms was broadened due to collisions in the collimation tube. This broadening reduces the centerline intensity and thus reduces the fraction of atoms that can be captured by the MOC. Between 343 and 433 K the width of the velocity distribution increases by a factor 2 suggesting that the capturable fraction decreases by a factor 4. The effects of a lower flux and a broader transverse velocity distribution from the collimated Knudsen source can explain most of the difference between the results from the measurement without a magnetic gradient and the scaling law. The additional limiting of density in the experiment in which the magnetic field is enabled can not be explained by effects caused by the collimated Knudsen source. However as can be seen from the results, at high temperatures the beam density approaches $10^{16}\,\mathrm{m}^{-3}$ which is the density in which in MOTs collisions between excited and ground state atoms and radiation trapping effects start to play a role [29–31]. More advanced laser cooling schemes using a repumper laser beam that has a dark spot in the very center of the atomic beam may allow overcoming this limitation [31]. Because of the added complexity this was not pursued in this experiment.

Ultimately, a beam density of $\left(6^{+3}_{-2}\right)\times10^{15}\,\mathrm{m}^{-3}$ was reached. This translates in a beam flux equivalent of $\left(0.6^{+0.3}_{-0.2}\right)$ nA through the selection aperture and an equivalent brightness of $\left(6^{+5}_{-2}\right)\times10^{6}\,\mathrm{A/(m^2\,sr\,eV)}$. The current Knudsen source does not allow for higher temperatures than ≈443 K. However, linear extrapolation of the measurement teaches that only a 20 % increase in density, and thus brightness, can be achieved when the source temperature is raised by 20 K. Since part of the deviation from the scaling law is caused by collisions inside the collimation tube of the Knudsen source a slightly higher flux can be expected when using a Knudsen source collimated by an aperture instead of a tube or the more complex candlestick oven design [32]. However, ultimately the density will be limited by the earlier mentioned effects.

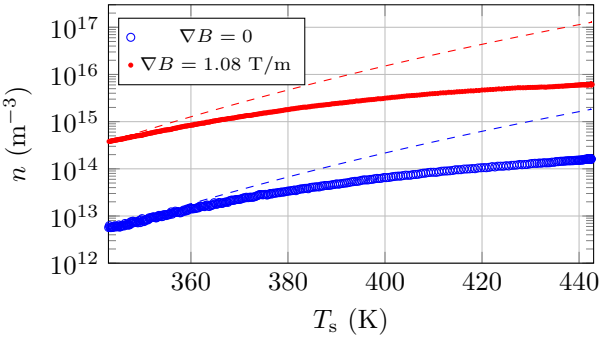

FIG. 8. Atomic beam density after the MOC as a function of the source temperature. Two measurements are shown: one in which only cooling is applied (∇B=0 T/m, the blue open circles) and one in which compression is applied (∇B=1.1 T/m, red dots). In all measurements the detuning of the cooling laser was set to -1.1 Γ and the detuning of the probe laser was set to 0 MHz. As a reference, the dashed lines show a scaling of the first data point with the theoretical flux comming from the Knudsen source under the assumption of no collissions inside the collimation tube [21].

IV. CONCLUSION

The properties of an atomic rubidium beam resulting from direct magneto-optical compression of effusive atoms from a collimated Knudsen source are evaluated. Laser-induced fluorescence is used to image the beam and determine its flux and transverse temperature. As for both of these parameters knowledge of the longitudinal velocity of the atoms was required, the longitudinal velocity distribution was measured as well. The average longitudinal velocity was found to be dependent on the magnetic field gradient in the magneto-optical compressor and had a value of 50-100 m/s. As the beam is intended to be photoionized and applied as a source for a focused ion beam, its flux is expressed in units of current and also the equivalent reduced brightness is calculated. In a single magneto-optical compression step the maximum equivalent beam current found was $\left(0.6^{+0.3}_{-0.2}\right)$ nA and the transverse temperature was $\left(0.2^{+0.1}_{-0.07}\right)$ mK. Together these values combine into an equivalent transverse reduced brightness of $\left(1^{+0.8}_{-0.4}\right)\times10^{6}\,\mathrm{A/(m^2\,sr\,eV)}$. With an additional sub-Doppler cooling step this value was increased to $\left(6^{+5}_{-2}\right)\times10^{6}\,\mathrm{A/(m^2\,sr\,eV)}$ by lowering the transverse temperature of the beam. When ionized, this would be a 6× improvement over the brightness of the liquid metal ion source, 300× larger than any MOT based ion source [13, 33] and similar to the estimated brightness from the $2D^+$ MOT based source by Knuffman et. al [16].

In future research the photoionization of the atomic beam will be investigated. To reach a high ionization degree, in order to conserve the high transverse reduced brightness, an ionization laser intensity of the order of $10^{11}\ \mathrm{W/m^2}$ is needed [18]. In order to reach this intensity a build-up cavity will be used to enhance the laser

power. By immediately accelerating the ions and focusing it, nanometer size waists are expected with a 30 keV beam containing 1 pA [19].

ACKNOWLEDGMENTS

This research is supported by the Dutch Technology Foundation STW, which is part of the Netherlands Organisation for Scientific Research (NWO), and which is partly funded by the Ministry of Economic Affairs. The research was also supported by FEI Company, Pulsar Physics and Coherent Inc. We would like to thank Bas van der Geer and Eddy Rietman for their design work on the magnetic quadrupole, and Eddy Rietman, Harry van Doorn and Iman Koole for their technical support.

Appendix: Uncertainty analysis

In linear uncertainty analysis the dependence of the end results on its parameters is linearized. This gives wrong results if the relative errors, $\Delta i/i$ are large. Therefore the upper and lower (systematic) value for the flux, temperature and brightness were calculated differently by filling in the parameters plus or minus their uncertainty margin in such a way that the maximal or minimal value for the flux, temperature or brightness was found. The complete equation used for finding the transverse temperature from the experiment is given by

$$T_x = \frac{m}{k_\mathrm{B}} \cdot \frac{\widetilde{v_z}^{\,2}}{(\Delta z)^2} \left(\frac{o^2\, l_\mathrm{px}^2}{b^2} \cdot \sigma_\mathrm{px}^2 - (R/2)^2 \right), \qquad \text{(A.1)}$$

in which σ_px is the root-mean-square width of the fitted normal distribution in units of camera pixels and l_px is the width of a single pixel. The complete equation for the flux was find by combining equations 3-5, resulting in

$$\Phi = \frac{4}{\Gamma} \cdot \frac{b\,\overline{v_z}\,o\,C}{l_\mathrm{img}\,\rho_{ee}\,(\delta_p)\;r_l^2\,t_\mathrm{c}\,T_w\,T_f\,G}, \qquad \text{(A.2)}$$

in which l has been substituted with $l = l_\mathrm{img}\frac{o}{b}$, in which l_img is the longitudinal size of the image. Using the same substitution and equation 6 for the density results in,

$$n = \frac{4}{\pi\Gamma} \cdot \frac{b\,o\,C}{R^2 l_\mathrm{img}\,\rho_{ee}\,(\delta_p)\;r_l^2\,t_\mathrm{c}\,T_w\,T_f\,G}. \qquad \text{(A.3)}$$

The complete equation for the equivalent brightness can be found by combining equation 7, A.1 and A.2 resulting in

$$B_r = \frac{4\,e}{m\,\pi^2\,\Gamma} \cdot \frac{b^3\,o\,(\Delta z)^2}{R^2\,l_\mathrm{img}\,\rho_{ee}\,(\delta_p)\;r_l^2\,t_\mathrm{c}\,T_w\,T_f\,G} \cdot \frac{C\,\overline{v_z}}{\widetilde{v_z}^{\,2}\;\left(o^2\,l_\mathrm{px}^2\,\sigma_\mathrm{px}^2 - b^2\,(R/2)^2\right)}. \qquad \text{(A.4)}$$

Typical values of all parameters used, are given in table I together with the uncertainties in them. With these values the relative uncertainties are +62 % and -37 % for the temperature, +51 % and -32 % for the flux, +48 % and -31 % for the density and +80 % and -30 % for the equivalent brightness.

[1] J. Weiner, V. Bagnato, S. Zilio, and P. Julienne, Rev. Mod. Phys. **71**, 1 (1999).
[2] A. D. Cronin, J. Schmiedmayer, and D. E. Pritchard, Rev. Mod. Phys. **81**, 1051 (2009).
[3] K. Dieckmann, R. Spreeuw, M. Weidemüller, and J. Walraven, Phys. Rev. A **58**, 3891 (1998).
[4] S. Chaudhuri, S. Roy, and C. S. Unnikrishnan, Phys. Rev. A **74**, 1 (2006).
[5] F. Lison, P. Schuh, D. Haubrich, and D. Meschede, Phys. Rev. A **61**, 1 (1999).
[6] W. DeGraffenreid, J. Ramirez-Serrano, Y.-M. Liu, and J. Weiner, Rev. Sci. Instrum. **71**, 3668 (2000).
[7] J. J. McClelland, A. V. Steele, B. Knuffman, K. A. Twedt, A. Schwarzkopf, and T. M. Wilson, Appl. Phys. Rev. **3** (2016).
[8] J. Orloff, Rev. Sci. Instrum. **64**, 1105 (1993).
[9] V. Raffa, P. P. Castrataro, A. Menciassi, and P. Dario, in *Appl. Scanning Probe Methods II - Scanning Probe Microsc. Tech.* (Springer, 2006).
[10] C. W. Hagen, E. Fokkema, and P. Kruit, J. Vac. Sci. Technol. B **26**, 2091 (2008).
[11] A. E. Bell, K. Rao, G. A. Schwind, and L. W. Swanson, J. Vac. Sci. Technol. B **6**, 927 (1988).
[12] J. Orloff, J. Vac. Sci. Technol. B **14**, 3759 (1996).
[13] J. Hanssen, S. Hill, J. Orloff, and J. McClelland, Nano Lett. **8**, 2844 (2008).
[14] M. P. Reijnders, P. A. van Kruisbergen, G. Taban, S. B. van der Geer, P. H. A. Mutsaers, E. J. D. Vredenbregt, and O. J. Luiten, Phys. Rev. Lett. **102**, 034802 (2009).
[15] B. G. Freinkman, A. V. Eletskii, and S. I. Zaitsev, Microelectron. Eng. **73-74**, 139 (2004).
[16] B. Knuffman, A. V. Steele, and J. J. McClelland, J. Appl. Phys. **114**, 44303 (2013).
[17] L. Kime, A. Fioretti, Y. Bruneau, N. Porfido, F. Fuso, M. Viteau, G. Khalili, N. Santic, A. Gloter, B. Rasser, P. Sudraud, P. Pillet, and D. Comparat, Phys. Rev. A **88**, 33424 (2013).
[18] S. H. W. Wouters, G. ten Haaf, R. P. M. J. W. Notermans, N. Debernardi, P. H. a. Mutsaers, O. J. Luiten, and E. J. D. Vredenbregt, Phys. Rev. A **90**, 063817 (2014).
[19] G. ten Haaf, S. H. W. Wouters, S. B. van der Geer, E. J. D. Vredenbregt, and P. H. A. Mutsaers, J. Appl. Phys. **116**, 244301 (2014).
[20] M. Viteau, M. Reveillard, L. Kime, B. Rasser, P. Sudraud, Y. Bruneau, G. Khalili, P. Pillet, D. Comparat,

TABLE I. Typical experimental parameters and their systematic uncertainties

Parameters (unit)	**Symbol**	**Value ± error**
Probe laser detuning (MHz)	δ_p	0.0 ± 0.1
Probe laser beam intensity (W/m^2)	I	96 ± 10
Saturation parameter for linear polarized light (W/m^2)	I_{sat}	31.8 + 7.2 - 0.0
Drift distance (m)	Δz	0.20 ± 0.02
Camera shutter time (s)	t_{c}	1.000 ± 0.001
Camera gain (counts/photon)	G	2.08 ± 0.08
Camera pixel size (μm)	l_{px}	5.86
Longitudinal image size (mm)	l_{img}	1.172
Probe window transmission (%)	T_{w}	90 ± 2
Filter transmission (%)	T_f	89 ± 1
Selection aperture radius (μm)	R	50 ± 1
Lens object distance (m)	o	0.237 ± 0.005
Lens image distance (m)	b	0.105 ± 0.005
Lens aperture radius (mm)	r_l	6 ± 0.5
Inverse averaged longitudinal velocity (m/s)	$\overline{v_z}$	85 ± 5
Inverse squared averaged longitudinal velocity (m/s)	$\widetilde{v_z}$	75 ± 5

I. Guerri, A. Fioretti, D. Ciampini, M. Allegrini, and F. Fuso, Ultramicroscopy **164**, 70 (2016).

[21] S. H. W. Wouters, G. ten Haaf, P. H. A. Mutsaers, and E. J. D. Vredenbregt, Rev. Sci. Instrum. **87**, 083305 (2016).

[22] J. Nellessen, J. Werner, and W. Ertmer, Opt. Commun. **78**, 300 (1990).

[23] Point Grey GS3-U3-23S6M.

[24] G. C. Bjorklund, M. D. Levenson, W. Lenth, and C. Ortiz, Appl. Phys. B **32**, 145 (1983).

[25] Toptica mFALC.

[26] D. A. Steck, "Rubidium 85 and 87 D Line Data," available online at http://steck.us/alkalidata/ (2013).

[27] C. J. Foot, *Atomic Physics* (Oxford University Press, 2005).

[28] O. J. Luiten, B. J. Claessens, S. B. Van Der Geer, M. P. Reijnders, G. Taban, and E. J. D. Vredenbregt, Int. J. Mod. Phys. A **22**, 3882 (2007).

[29] C. D. Wallace, T. P. Dinneen, K. Y. N. Tan, T. T. Grove, and P. L. Gould, Phys. Rev. Lett. **69**, 897 (1992).

[30] T. Walker, D. Sesko, and C. Wieman, Phys. Rev. Lett. **64**, 408 (1990).

[31] W. Ketterle, K. B. Davis, M. A. Joffe, A. Martin, and D. E. Pritchard, Phys. Rev. Lett. **70**, 2253 (1993).

[32] M. R. Walkiewicz, P. J. Fox, and R. E. Scholten, Rev. Sci. Instrum. **71**, 3342 (2000).

[33] N. Debernardi, R. W. L. van Vliembergen, W. J. Engelen, K. H. M. Hermans, M. P. Reijnders, S. B. van der Geer, P. H. A. Mutsaers, O. J. Luiten, and E. J. D. Vredenbregt, New J. Phys. **14**, 083011 (2012).